ACS APPLIED MATERIALS & INTERFACES

Research Article

www.acsami.org

# Interconnected Tin Disulfide Nanosheets Grown on Graphene for Li-Ion Storage and Photocatalytic Applications

Peng Chen, Yun Su, Hong Liu,* and Yong Wang*

Department of Chemical Engineering, School of Environmental and Chemical Engineering, Shanghai University, Shangda Road 99, Shanghai, P. R. China, 200444

Supporting Information

**ABSTRACT:** Reduced graphene oxide (RGO) nanosheet-supported $SnS_2$ nanosheets are prepared by a one-step microwave-assisted technique. These $SnS_2$ nanosheets are linked with each other and dispersed uniformly on RGO surface. The $SnS_2$-RGO sheet-on-sheet nanostructure exhibits good electrochemical performances as an anode material for lithium ion batteries. It shows larger-than-theoretical reversible capacities at 0.1 *C* and excellent high-rate capability at 1 *C* and 5 *C*. The composite is also for the first time identified as an excellent visible light-driven catalyst of rhodamine B and phenol with high degradation efficiencies. The removal rates of rhodamine B and phenol are 100 and 83.2%, respectively, for the $SnS_2$-RGO composite, whereas these values are only 64.8 and 51.5% for pristine $SnS_2$ after the same irradiation times. The outstanding electrochemical or photocatalytic performances of the composite have been attributed to the complementary effect of RGO and $SnS_2$ in the perfect sheet-on-sheet composition nanostructure.

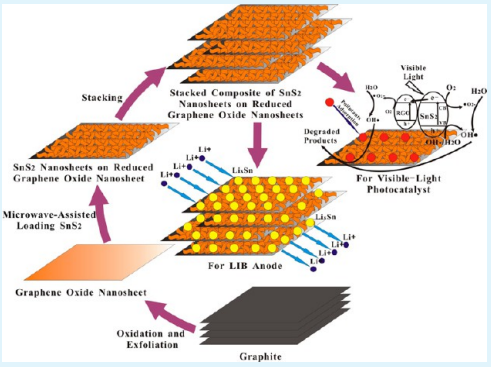


**KEYWORDS:** *reduced graphene oxide, $SnS_2$ nanosheet, sheet-on-sheet, lithium ion batteries, photocatalyst*

## 1. INTRODUCTION

Energy deficiency and environmental pollution are two major challenges for sustainable development of modern society, which requires innovative research of the materials design and the improvement of their energy-storage and environmental properties. As one of the most important metal-sulfide materials, tin disulfide has a layered $CdI_2$-type structure, which is composed of a tin cation sandwiched between two layers of sulfur anions. In recent years, tin disulfide has attracted intensive interest for electrical storage in Li-ion batteries[1−15] and as photocatalysts for pollutant degradation.[16−31]

Tin disulfide is a promising anode for Li-ion batteries to meet the increasing demands for advanced electrical devices or vehicles because it has a large theoretical capacity of 645 mAh $g^{-1}$, which is substantially larger than commercial graphite anode (372 mAh $g^{-1}$). However, their cycliablities are usually poor because there is a critical problem of large volume change and electrode pulverization for tin-based anodes. Since its discovery in 2004, graphene-supported composite anode materials have been proposed as an effective solution to solve the problem.[32−54] This is because graphene is flexible, robust, highly-conductive, and therefore suggested as a promising matrix to be composited with other high-capacity electrodes materials.[32−56] The mechanical stress associated with volume change can be relieved by the presence of graphene to a large extent. On the other hand, the unique properties relative to few-layer graphene can be also improved because the restacking of graphene to graphite platelets can be largely hindered by the sandwiched materials between graphene nanosheets (GNS). Several studies have been reported on the synthesis of $SnS_2$-graphene composites with usually two $SnS_2$ morphologies: nanoparticle-on-sheet[43−49] and nanoplate-on-sheet.[50−54] These composites were usually prepared by hydrothermal or solvothermal method,[43−53] except that an interesting chemical vapor deposition (CVD) technique was used to prepare $SnS_2$-graphene nanoplate-on-sheet structure with substantially enhanced Li-ion storage properties.[54] The presented interconnected $SnS_2$ nanosheet grown on graphene in this work has not been reported previously.

Nowadays there has been increasing interest in the application of semiconductors as photocatalysts to degrade organic pollutants, such as rhodamine B (RhB) and phenol, which are detrimental to the environment. By virtue of its low cost, high photocatalytic activity, and good biocompatibility, $TiO_2$ is widely used as photocatalysts. However, because of its wide band gap (3.2 eV), it is not active under visible light irradiation, which accounts for 46% of the total solar energy.[57] To meet this demand, the semiconducting metal sulfides have been investigated as a class of candidates for photocatalysts under visible light. Compared with $TiO_2$ (3.2 eV), $SnS_2$ has a narrower band gap of ∼2.2 eV, which makes it more sensitized for visible light. Moreover, $SnS_2$ is inexpensive, chemically stable and environmental-friendly, and therefore has been reported as a promising visible light-driven photocatalyst for

Received: September 10, 2013
Accepted: October 24, 2013
Published: October 24, 2013

  

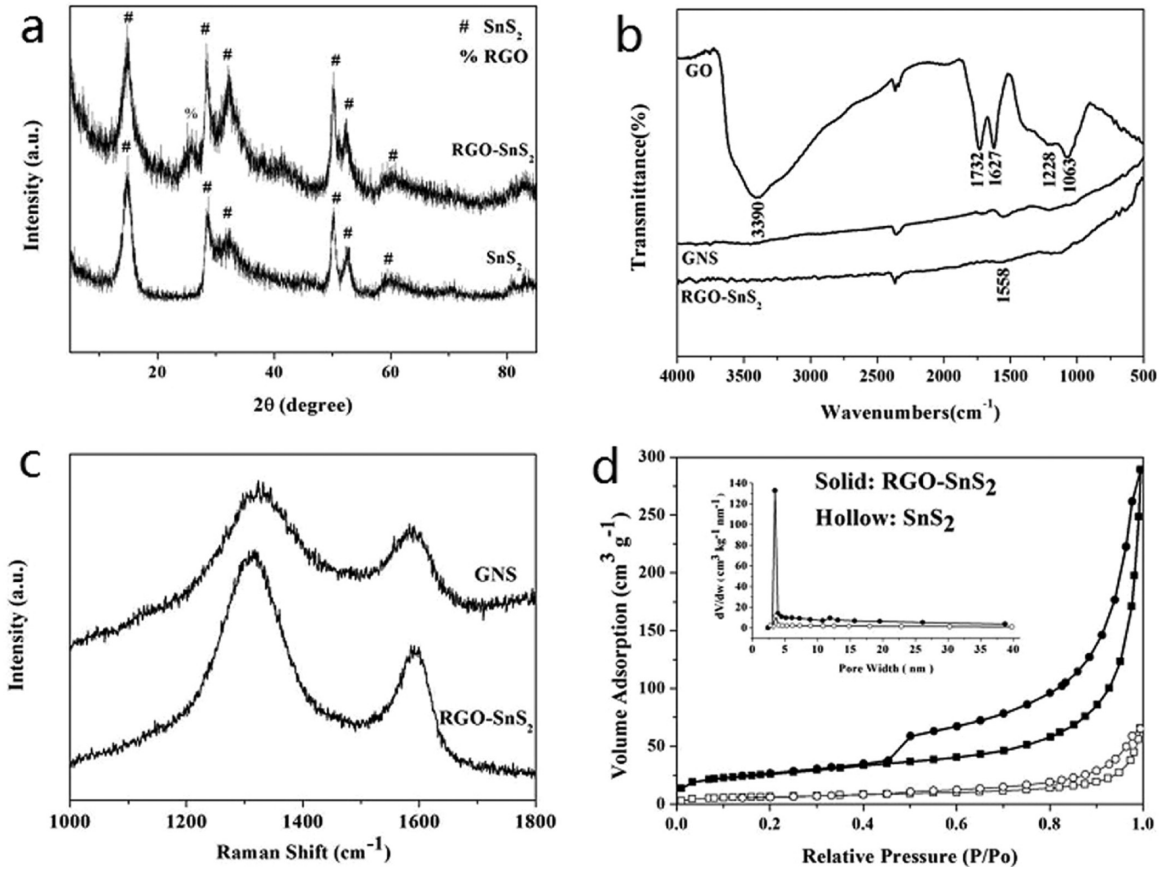


**Figure 1.** (a) XRD patterns of $SnS_2$ and $SnS_2$-RGO composite. (b) FTIR spectra of GO, GNS, and $SnS_2$-RGO composite. (c) Raman spectra of GNS and $SnS_2$-RGO composite. (d) $N_2$ adsorption−desorption isotherm of $SnS_2$-RGO composite. The inset shows the pore size distribution calculated from the desorption branch.

pollutant degradation.[16−31] It is suggested that if composited with graphene nanosheets, the $SnS_2$ photocatalyst should own a larger specific surface area, which can benefit the absorption and transportation for pollutant molecules and facilitate the rapid diffusion during the reaction. Moreover, the unique 3D structure of composite may provide more reaction sites to enhance the photocatalytic efficiency. For these reasons, the $SnS_2$-graphene composite should be a promising visible light-driven photocatalyst to degrade organic pollutants. However, to the best of our knowledge, there is no report about the $SnS_2$-graphene composite as photocatalyst in the degradation of organic pollutants.

Herein, a new $SnS_2$-graphene sheet-on-sheet nanostructure, namely reduced graphene oxide (RGO) nanosheets supported $SnS_2$ nanosheets, is designed and prepared by a fast microwave-assisted technique in this work. The primary objective of our structure design is that the $SnS_2$ nanosheet structure is suggested as the perfect structure to be composited with graphene nanosheets basically because they are both two dimensional nanostructures and should have the best structure affinity. In this work, the obtained $SnS_2$-RGO sheet-on-sheet composite showed large capacities at both low and high current rates as an anode for lithium-ion batteries and excellent high photodegradation rates of the RhB and phenol pollutants under visible-light irradiation.

## 2. EXPERIMENTAL SECTION

**2.1. Preparation of $SnS_2$-RGO Sheet-on-Sheet Nanostructure.** Graphene oxide was synthesized from natural graphite powder with a modified Hummers method as reported elsewhere previously.[32,33] Graphite nanopowders (XF NANO, 40 nm in thickness) was used as the starting graphite to be exfoliated. In a typical process, 10 ml of 0.3 M $SnCl_4{\cdot}5H_2O$ ethylene glycol solution and 10 ml of 0.6 M thiourea ($CH_4N_2S$) ethylene glycol solution were mixed to form a transparent solution after strong magnetic stirring for 10 min. 0.28 g graphene oxide (GO) was dispersed in 40 ml ethylene glycol under ultrasonic irradiation and then added to the above mixture solution. The mixture was sealed in a specialized glass tube under microwave irradiation at 180 °C for 20 min in a single mode microwave reactor (Nova, EU Microwave Chemistry). The precipitates were collected after centrifuging and copious washing with ethanol. After drying in an electrical oven at 60 °C, $SnS_2$-reduced graphene oxide (RGO) composite was obtained. The pristine $SnS_2$ material was prepared by a similar procedure except for the absence of GO materials.

**2.2. Materials Characterization.** The obtained products were characterized with X-ray diffraction (XRD, Rigaku D/max-2550 V, Cu K$\alpha$ radiation), field-emission scanning electron microscopy (FE-SEM, JSM-6700F) with an energy-dispersive X-ray spectrometer (EDS) and transmission electron microscopy/selected area electron diffraction (TEM/SEAD, JEOL JEM-200CX and JEM-2010F) in the Instrumental Analysis and Research Center of Shanghai University. Raman spectroscopy was recorded on Renishaw in plus laser Raman spectrometer (excitation wavelength = 785 nm, excitation power = 3 mW, spot size ≈ 1.2 $\mu$m). Fourier transform infrared (FTIR) spectra were measured by a BIO-RAD FTS 135 FTIR spectrophotometer using the KBr pellet method. The contents of carbon and sulfur elements were collected by a high-frequency infrared carbon sulfur analyzer (Keguo Instrument, HC-500P). The electrical conductivity was measured by a four-electrode method using a conductivity detection meter (Shanghai Fortune Instrument, FZ-2010).

**2.3. Electrochemical Measurement.** The working electrodes were composed of 80 wt % active material, 10 wt % the conductivity agent (acetylene black), and 10 wt % the binder (poly vinylidene difluoride, PVDF, Aldrich). Lithium foil (China Energy Lithium Co., Ltd) was used as counter and reference electrode. The electrolyte was 1 M $LiPF_6$ in a 50:50 w/w mixture of ethylene carbonate (EC) and diethyl carbonate (DEC). Electrochemical measurements were performed on a LAND-CT2100 test system. The Swagelok-type cells were discharged and charged at a constant current (66 mA $g^{-1}$, 0.1 C, 1 C = 660 mA $g^{-1}$) in the fixed voltage range 5 mV-3 V. The loading amount of the electrode was kept at ~1.5 mg $cm^{-2}$. High rates of 1 C and 5 C were also used and the first cycle discharging was kept at 0.1 C. Cyclic voltammetry (CV) was carried out on CH Instruments electrochemical workstation (model 660D) at a scan rate of 0.1 mV $s^{-1}$.

**2.4. Photocatalytic Test.** Photocatalytic activities of the samples were evaluated by the photocatalytic degradation of different pollutants (rhodamine B and phenol) in an aqueous solution under visible-light irradiation. The photocatalytic system included a 500W Xe arc lamp with a UV TUTOFF FILTER ($\lambda$>420 nm), circulation of water through an external cooling coil and a ventilating fan, which were used to prevent any thermal catalytic effects. All experiments were conducted at room temperature in air. In a typical photocatalytic experiment, 0.05 g photocatalyst was added into 50 ml pollutant solution (10 mg $L^{-1}$) in a reaction cell with a Pyrex jacket. Prior to irradiation, the suspension was magnetically stirred in the dark for 1 h to reach an adsorption-desorption equilibrium of the pollutant on the catalyst surface. Then these suspensions were exposed to visible-light irradiation under magnetic stirring. At given time intervals, about 5 ml suspensions were collected and centrifuged (13 000 rpm, 15 min) to remove the photocatalyst particles. The pollutant concentration of the obtained solution was analyzed by a UV-VIS spectrophotometer (Hitachi, U-3310) by checking the absorbance at 553 nm and 270 nm for RhB and phenol, respectively.

## 3. RESULTS AND DISCUSSION

**3.1. Materials Synthesis and Characterization.** The XRD patterns of pristine $SnS_2$ and $SnS_2$-reduced graphene oxide (RGO) composite are shown in Figure 1a. There is a small diffraction peak at 25.8° for $SnS_2$-RGO composite, which is an indication of the presence of reduced graphene oxide in the composite. The corresponding interplanar spacing of RGO was calculated to be 0.346 nm, which is slightly larger than that of standard graphite (0.335 nm). A few other characteristic peaks in the as-prepared pristine $SnS_2$ and $SnS_2$-RGO composite can be readily ascribed to $SnS_2$ with hexagonal layered structure (PDF 23-0677). The FTIR spectra of GO, GNS and $SnS_2$-RGO composite are shown in Figure 1b. The peak at 3390 $cm^{-1}$ of GO could be attributed to the stretching vibration of adsorbed water molecules and surface −OH groups. The peaks of 1732 and 1228 $cm^{-1}$ were related to the presence of abundant O═C and O−C functional groups on the surface of graphene oxide nanosheets. After a microwave-assisted process, these peaks were largely weakened in the $SnS_2$-RGO composite, indicating the reduction of GO. The successful reduction of GO to RGO can be further confirmed by the XRD patterns in the Supporting Information in Figure S1. The characteristic peak of GO at ~11° has been shifted to ~25°. For GNS and $SnS_2$-RGO composite, the stretch appeared at 1558 $cm^{-1}$ in Figure 1b could be ascribed to the skeletal vibration of graphene nanosheets.[58] It is suggested that these oxygen-contained groups may facilitate the absorption and binding of $SnS_2$ nanostructures on the RGO surface.

The Raman spectra of GNS and $SnS_2$-RGO composite are shown in Figure 1c. The intensity ratio ($I_D$:$I_G$) of the D band (located at 1325 $cm^{-1}$) to G band (located at 1590 $cm^{-1}$) for $SnS_2$-RGO composite is about 1.41, which is higher than that of bare graphene nanosheets. The more disordered carbon structure in $SnS_2$-RGO composite may be attributed to the defects generated by the insertion of $SnS_2$ nanosheets into graphene layers. These defects may be beneficial to the more lithium diffusion route and enhanced lithium-ion storage capacity. The results of Brunauer−Emmett−Teller (BET) analysis of $SnS_2$-RGO composite and $SnS_2$ nanoflowers with the nitrogen adsorption-desorption isotherm are shown in Figure 1d. The well-defined steps of the isotherm illustrate the mesoporous structure of $SnS_2$-RGO composite. The BET surface area of $SnS_2$-RGO composite was measured to be 92.1 $m^2$ $g^{-1}$, which is much larger than the value of $SnS_2$ nanoflowers (22.3 $m^2$ $g^{-1}$). Both pristine $SnS_2$ nanoflowers and $SnS_2$-RGO composite exhibit a similar average pore size of ~3.5 nm (BJH analysis, the inset of Figure 1d). Compared to pristine $SnS_2$ nanoflowers, the enhanced specific surface area of the composite can accelerate lithium diffusion during cycling and enlarge the inner space for absorption or desorption of degradation pollutant, which enhance greatly electrochemical performance and photocatalytic efficiency of the composite.

FESEM images in Figure 2 show the surface morphologies and microstructure of $SnS_2$ nanoflowers (Figure 2a, b), reduced graphene oxide nanosheets supported $SnS_2$ nanosheets (Figure 2c, d), and graphene nanosheets (GNS, Figure 2f). A number of pristine $SnS_2$ flower-like microspheres (~500−600 nm in size) are observed in Figure 2a, b, which are composed of many nanosheet-like "flower leaves". In the presence of graphene oxide, the $SnS_2$ nanoflowers were unfolded and distributed uniformly as continuous wrinkled nanosheets on the surface of RGO nanosheets (Figure 2c, d). This change should be ascribed to the important effect of surface groups of GO on the crystal growth and self-assembly process of $SnS_2$ materials. Bare

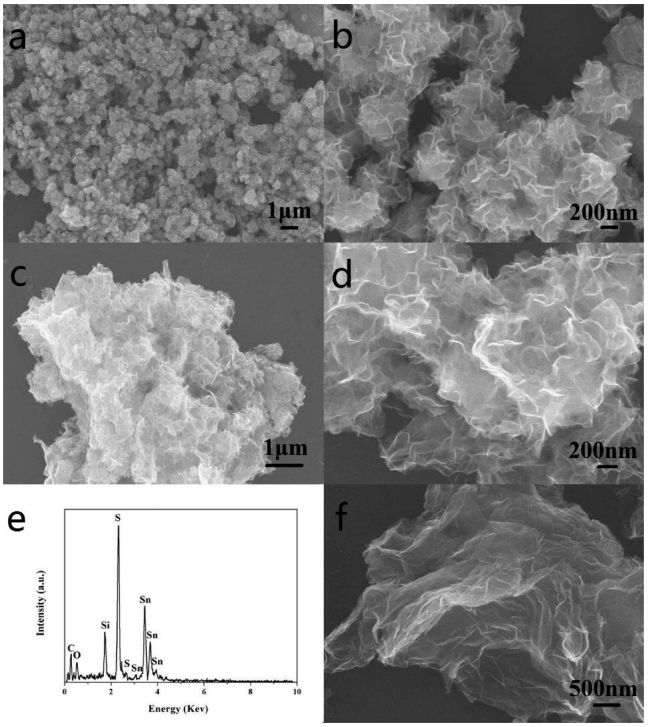


**Figure 2.** SEM images of (a, b) pristine $SnS_2$ nanoflower microspheres, (c, d) $SnS_2$-RGO sheet-on-sheet composite, (e) the EDS spectrum of $SnS_2$-RGO composite, (f) bare graphene nanosheets.

GNS are observed as few-layer stacking of single graphene nanosheet (Figure 2f). The EDS results of the $SnS_2$-RGO sheet-on-sheet composite are shown in Figure 2e. A few elements such as C, O, Sn, S, and Si are observed in the composite. The Si substrate was used to disperse the samples for SEM measurement, which can remove the carbon effect from the commonly used substrate of carbon paste. The composite was also measured by a high-frequent infrared carbon analyzer. The elemental analysis revealed that the carbon content was 31.6 wt% in $SnS_2$-RGO composite, which is slightly larger than the theoretical value (25 wt % carbon) based on the experimental calculation. The molar ratio of Sn:S was estimated to be ~1:2 in the composite by the energy dispersive spectra (EDS) results. Figure 3 shows the mapping images of

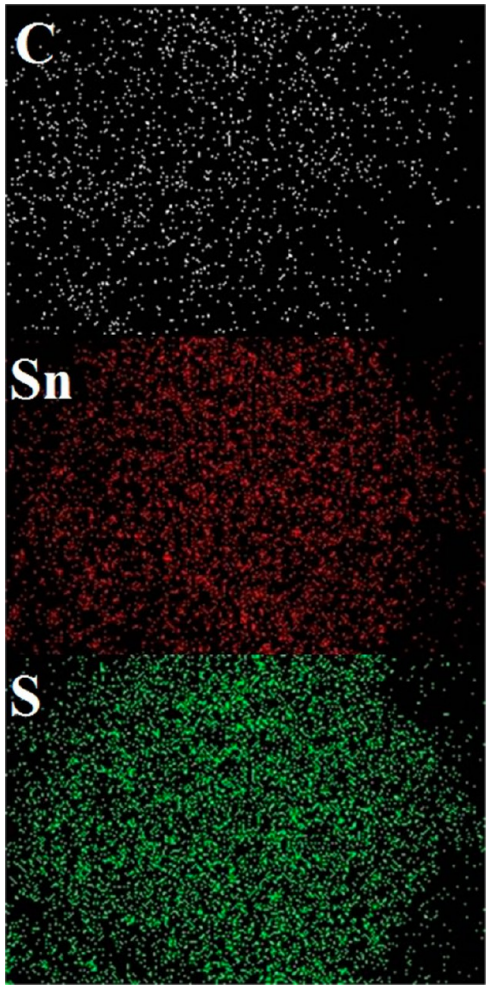


**Figure 3.** Elemental mapping images of $SnS_2$-RGO sheet-on-sheet composite for three elements of C, Sn, and S.

three elements C, Sn, and S in $SnS_2$-RGO composite. These evenly distributed points of C, Sn, and S elements further demonstrate the highly homogeneous composite composition and structure affinity between $SnS_2$ nanosheets and RGO nanosheets.

TEM images of GNS and $SnS_2$ nanoflowers are shown in images a and b in Figure 4, respectively. GNS are quite thin under electron imaging and can be confirmed by the HRTEM image of the cross-section in the inset image of Figure 4a. Pristine $SnS_2$ nanosheet-stacked nanoflowers are around 500–600 nm in size (Figure 4b). Figure 4c–e show TEM images of

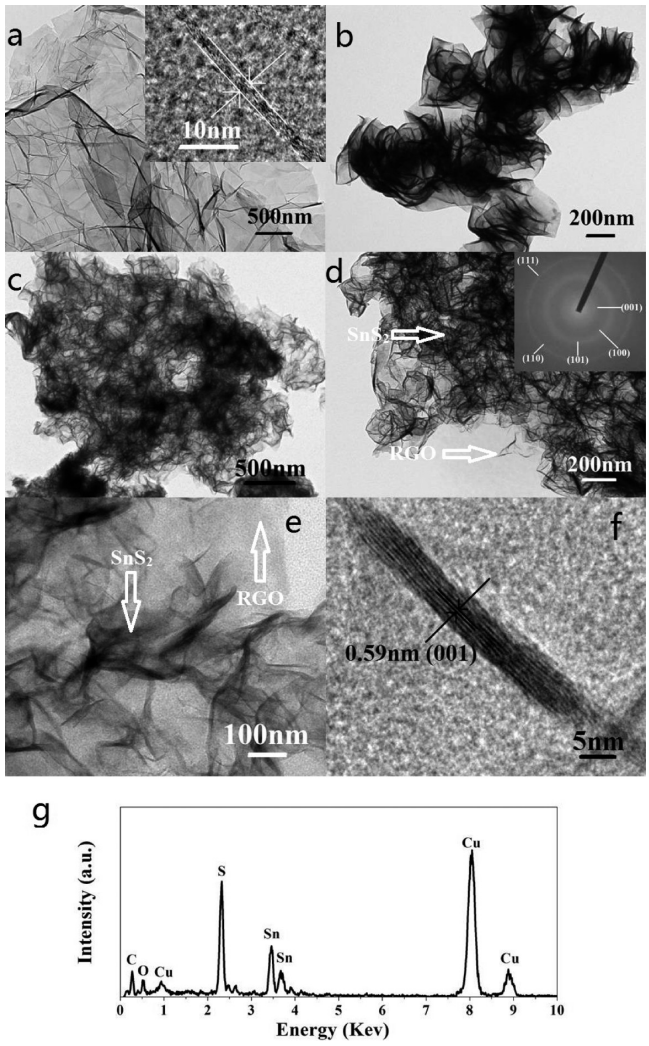


**Figure 4.** TEM images of (a) GNS, the inset image showing the cross-section, (b) pristine $SnS_2$, (c–e) $SnS_2$-RGO sheet-on-sheet composite. The inset image of (d) shows the SEAD pattern of polycrystalline $SnS_2$. (f) HRTEM image showing the cross-section of $SnS_2$ nanosheet in the $SnS_2$-RGO composite. (g) The EDS spectrum.

$SnS_2$-RGO sheet-on-sheet composite with different magnifications. As shown in Figure 4e, it is clear that the $SnS_2$ nanosheets are unfolded and distributed uniformly on the RGO surface. Notably, the $SnS_2$ nanosheets are not in flat contact with RGO surface, but exhibit many cross-sections of the wrinkled nanosheet structure. Therefore in this porous three dimensional sheet-on-sheet nanostructure, the specific surface area of the composite should be largely improved compared to the completely flat contact between $SnS_2$ and RGO. The distinct ring pattern of the selected-area electron diffraction (SEAD) is displayed in the inset of Figure 4d, which reveals the polycrystalline $SnS_2$ nanosheets structure. The HRTEM image in Figure 4f reveals a cross-section of $SnS_2$ nanosheet. An interlayer distance of 0.59 nm can be identified, which indicates the hexagonal $SnS_2$ layers stacked along the 001 direction. The EDS result in Figure 4g confirms the presence of S and Sn elements in the products as shown in the above TEM images.

A schematic sketch of growth process and applications of $SnS_2$-RGO composite is shown in Figure 5. In the presence of GO substrates, $SnS_2$ nanosheets are dispersed uniformly on the

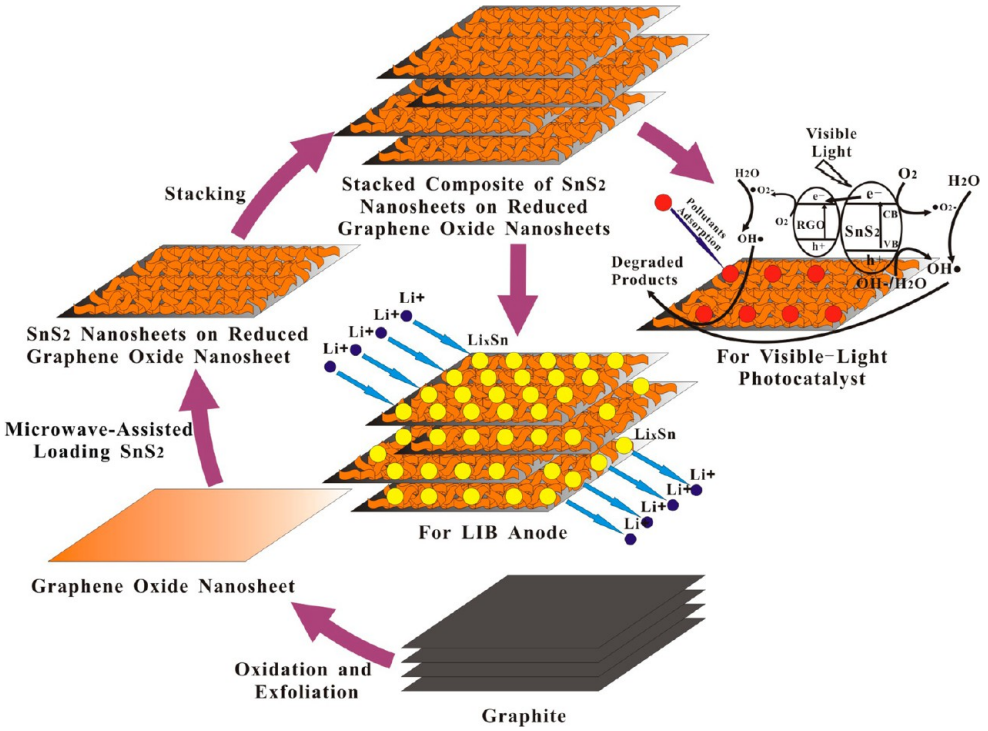


**Figure 5.** Schematic illustration of the growth process and applications of $SnS_2$–RGO sheet-on-sheet nanostructure.

surfaces of reduced graphene oxide nanosheets with a novel sheet-on-sheet morphology. On one hand, RGO could absorb and bind $SnS_2$ nanosheets and restraint their self-assembly into 3D flower-like morphology. As a buffering layer, RGO can alleviate the large volume change during the Li insertion and extraction process, which also improve electrical conductivity and mechanical stability of the composite. On the other hand, the existence of $SnS_2$ nanosheets between RGO nanosheets can prevent the restacking of few-layer graphene layers and preserve their intriguing properties relative only to their few-layer structure. Therefore, the composite may provide more reaction sites to enhance the photocatalytic efficiency. Moreover, the absorption and transportation for pollutant molecules and photoelectrons are also facilitated during the photocatalyzed reaction. Because of the complementary effect between RGO and $SnS_2$ nanosheets in the composite, it should exhibit excellent electrochemical properties and photocatalytic performances.

**3.2. Lithium-Ion Storage Properties.** Figure 6a shows the charge-discharge curves of pristine $SnS_2$ and $SnS_2$-RGO composite at a current density of 66 mA $g^{-1}$ (0.1 *C*, 1 *C* = 660 mA $g^{-1}$) in first and the 40th cycle. A long plateau was observed around 1.1 V for pristine $SnS_2$, which is ascribed to the decomposition of $SnS_2$ into metallic Sn and $Li_2S$ as well as the formation of solid electrolyte interface (SEI). There are two slopes observed at ~1.5 and 1.0 V for $SnS_2$-RGO composite, which agree well with the CV results in the Supporting Information, Figure S2. The voltage difference between $SnS_2$ and $SnS_2$-RGO should be mainly due to the presence of RGO. This phenomenon agrees well with previous $SnS_2$-RGO composites.[51] The initial charge capacity (lithium extraction) of $SnS_2$-RGO composites was 1077 mAh $g^{-1}$, which is substantially larger than the theoretical capacity calculation based on the physical addition of pristine $SnS_2$ (706 mAh $g^{-1}$) and bare GNS (727 mAh $g^{-1}$) . Although the mechanism for extremely high capacity is not very clear, it is believed that the extra amount of lithium ion may be stored in pores or microcavities (as confirmed in Figure 1d) on the surface of the disordered imperfect RGO structure (as confirmed in the Raman spectra of Figure 1c) and between the 3D sheet-on-sheet packed porous structure. The Li-ion storage has also been suggested by a possible faradic capacitance and absorption on both sides of RGO.[58−60] The discharge capacity (lithium insertion) of composite in first cycle was 1505 mAh $g^{-1}$, and therefore its Coulombic efficiency could be calculated to be 71.6%. The first-cycle capacity loss should be mainly ascribed to lithium ion consumption in the electrolyte decomposition and formation of solid electrolyte interface (SEI) film around electrode materials, which has a relatively large surface area of 92.1 $m^2$ $g^{-1}$.

The cyclic performances of pristine $SnS_2$ nanoflowers, GNS and $SnS_2$-RGO composite at 0.1 *C* and 1 *C* are shown in Figure 6. The charge capacity of the composite at 0.1 *C* was 896 mAh $g^{-1}$ after 40 cycles, which is higher than those of pristine $SnS_2$ (255 mAh $g^{-1}$) and GNS (373 mAh $g^{-1}$) after the same cycle number. The small capacity fading for the composite may be due to the partial trapping of lithium ions in the pores or microcavities on RGO surface, which cannot come out in the following cycles. Moreover, the large volume change associated with the formation of Li–Sn alloys may be not fully accommodated by the presence of RGO. The composite also exhibited a better cycling performance at a large current rate. At a constant current of 660 mA $g^{-1}$ (1 C), the initial charge capacity of composite was 934 mAh $g^{-1}$ (Figure 6e and Supporting Information, Figure S3), which decreased to 657 mAh $g^{-1}$ after 40 cycles. In comparison, pristine $SnS_2$ and GNS displayed smaller charge capacities of 247 mAh $g^{-1}$ and 371 mAh $g^{-1}$ after 40 cycles. Figure 6c and Figure 6f show the contribution of one component ($SnS_2$ or RGO) in the composite assuming that the other component (RGO or

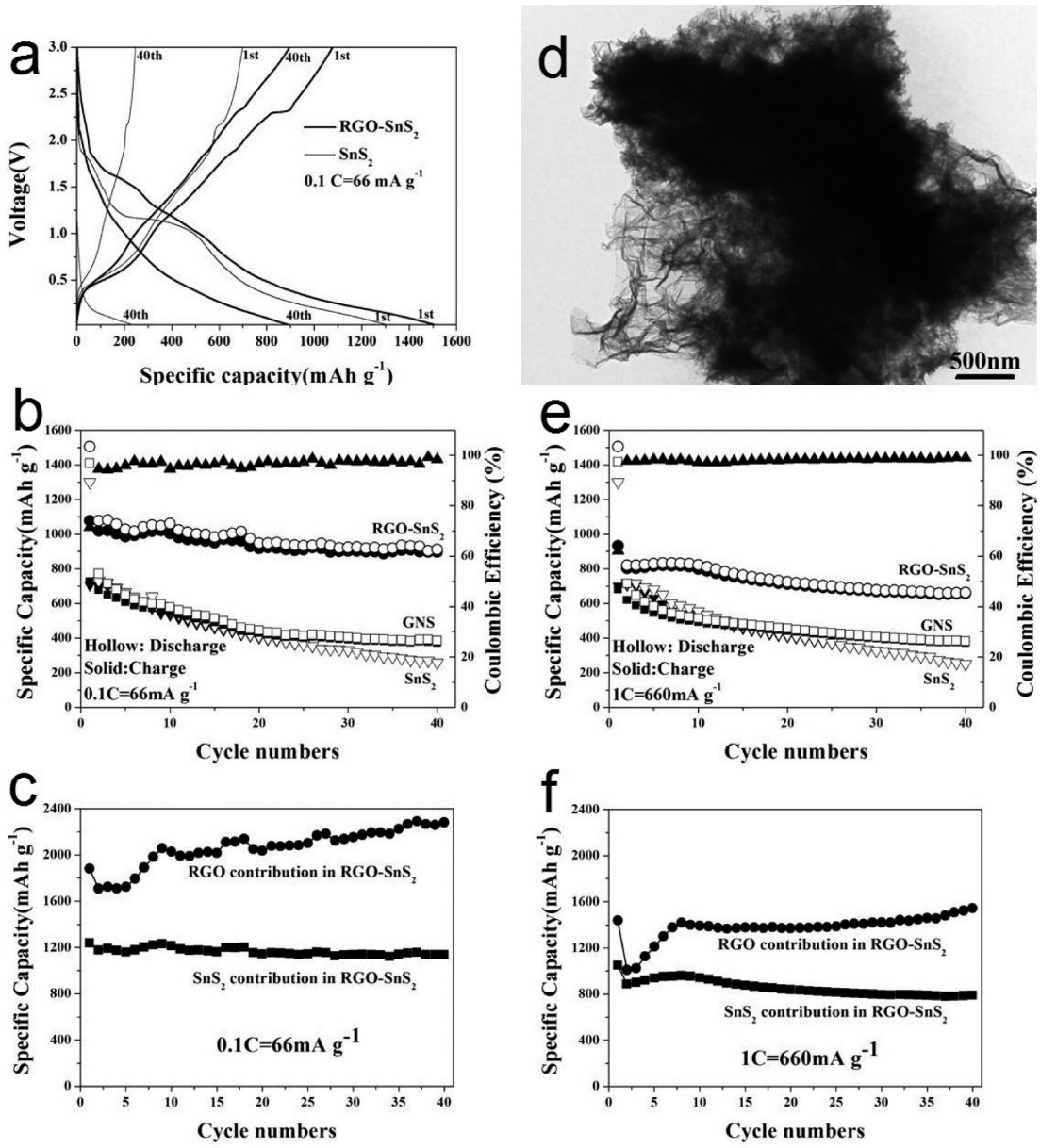


**Figure 6.** (a) Discharge (lithium insertion) and charge (lithium extraction) curves of the products at 0.1 C (1 *C* = 660 mA $g^{-1}$). (b) Cycling performances at 0.1 *C*. (c) The $SnS_2$ or RGO contribution in the composite, assuming the other one has no capacity improvement in the composite. (d) TEM image of the cycled electrode showing the stable sheet-on-sheet structure during cycling in the presence of carbon black and PVDF. (e) Cycling performances at 1 *C*. (f) The $SnS_2$ or RGO contribution in the composite at 1 *C*.

$SnS_2$) has no capacity improvement in the composite compared to bare RGO and pristine $SnS_2$. It is clear that both components exhibit better electrochemical performances in the composite and a distinct synergetic effect can be identified. $SnS_2$ contributed a stable capacity of ~1150 mAh $g^{-1}$ during 40 cycles. It is noted that the contribution of RGO in the composite is even larger with the increased cycle numbers (from ~1700 to ~2300 mAh $g^{-1}$ in 40 cycles). This is because the capacity improvement of $SnS_2$ in the composite is neglected in the calculation assumption. In fact, the cycling performances of pristine $SnS_2$ nanoflowers are worse than that of bare GNS as shown in panels b and e in Figure 6. Therefore the improvement of pristine $SnS_2$ in the composite would have a larger effect in the overall properties improvement of the composite. These large reversible capacities achieved for the $SnS_2$-RGO sheet-on-sheet electrode are also better than the graphene-$SnS_2$ composites reported recently,[44,45,53] in which comparable test current and voltage window were used and therefore these results can be compared on a fair basis. These excellent electrochemical performances of $SnS_2$-RGO composite should be largely attributed to a synergic effect between the graphene and $SnS_2$ nanosheets. First, the reduced graphene oxide nanosheets can act as a buffer layer to absorb mechanical stress induced by the volume change during cycling, which can maintain the stable electrode structure and electrochemical activities. Secondly, the electrical conductivity of $SnS_2$ in the composite is largely improved by the usage of graphene. As measured by a four-electrode method, $SnS_2$-RGO composite exhibits an electrical conductivity of 0.037 s $cm^{-1}$, which is more than one thousand times higher than pristine $SnS_2$ ($3.2 \times 10^{-5}$ s $cm^{-1}$). Thirdly, the porous 3D sheet-on-sheet electrode nanostructure may facilitate the lithium diffusion and electro-

lyte contact and offer more active sites for lithium ion storage. Lastly, the restacking of RGO nanosheets can be effectively hindered by $SnS_2$ nanosheets. Therefore, their intriguing properties such as high surface area and short lithium diffusion length can be preserved in long-term cycling and their lithium ion storage properties should be also enhanced substantially. The extremely high-rate (3300 mA $g^{-1}$, 5 *C*) electrochemical performances of $SnS_2$-RGO composite are also explored as shown in the Supporting Information of Figure S4. An initial high charge capacity of 854 mAh $g^{-1}$ was still achieved for the $SnS_2$-RGO sheet-on-sheet composite at this very high current rate. This capacity is around 79.3 and 91.4% of the values achieved at 0.1 *C* and 1 *C*, respectively. This high-rate capability has not been witnessed previously in the literature.[43−54] These excellent high-rate performances should be largely described to the enhanced electrical conductivity, facilitated lithium diffusion and improved structure stability in the perfect sheet-on-sheet composition structure.

**3.3. Photocatalytic Performances.** The photocatalytic degradation of rhodamine B (RhB) and phenol under visible light irradiation[61−69] was used to evaluate the photocatalytic performances of $SnS_2$-RGO composite. As a comparison, pristine $SnS_2$ or RGO was also tested under identical conditions. It can be seen from the curves of the pollutant absorption rates (Figure S5 in the Supporting Information) that the adsorption-desorption equilibrium of the pollutants on the catalyst surfaces have been almost achieved in 60 min before visible-light irradiation. The pollutant concentration after the adsorption-desorption equilibrium was used as the original concentration ($C_0$) for the degradation rates measurements. Therefore the influence of pollutant adsorption on the photocatalysts can be largely neglected in the photocatalytic process. Figure 7 shows that the pollutants of RhB and phenol can not be degraded under visible light irradiation in the absence of photocatalysts. It is indicated that these pollutants are stable in the test environment and the reaction mechanism for the pollutants degradation in this work is a photocatalytic process. In the presence of RGO, almost no RhB degradation was observed and phenol was slightly degraded. In comparison, the degradation rates were remarkably enhanced when $SnS_2$ and $SnS_2$-RGO were used as the photocatalysts. About 64.8% of RhB was decomposed after 120 min irradiation in the presence of pristine $SnS_2$, while this value reached almost 100% for the $SnS_2$-RGO composite (Figure 7a). On the other hand, the degradation rate of phenol was 51.5% for $SnS_2$ after 240 min irradiation, which increased to 83.2% for $SnS_2$-RGO composite after same irradiation time (Figure 7b). These results indicate clearly that the introduction of RGO can enhance the photocatalytic performance of $SnS_2$. Notably, the photocatalytic activity of the obtained $SnS_2$-RGO composite on the degradation of organic pollutant RhB and phenol is higher than $SnS_2$-based materials reported previously.[23,24,29] These photocatalytic properties are also better than various graphene-based composites[62−66,68,69] and comparable to CdS-RGO,[61] and $Bi_2WO_6$-RGO.[67] For detailed analysis of the photocatalysis kinetics of the pollutants degradation, the pseudo-first-order model was applied. This model is generally used for photocatalytic degradation process if the initial concentration of pollutant is low. The rate constants were evaluated from the data plotted in panels a and b in Figure 7 and summarized in Table 1. The rate constant for $SnS_2$-RGO composite to remove RhB is ~2.2 $h^{-1}$, which is ~4.4 times as large as that of pristine

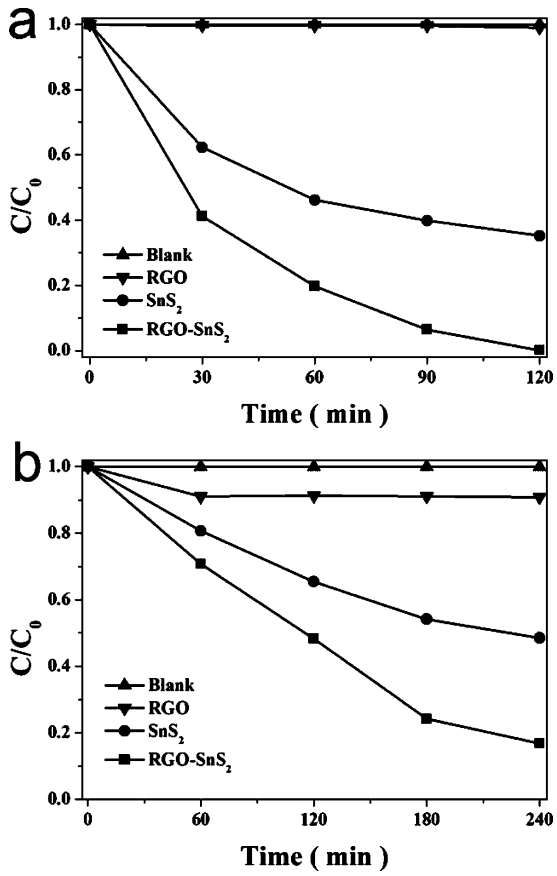


**Figure 7.** Photocatalytic activities of $SnS_2$, RGO, and $SnS_2$-RGO composite on the degradation of pollutants under visible-light irradiation: (a) RhB, (b) phenol.

**Table 1. Pseudo-first-order Rate Constants of the Catalytic Photodecomposition of Different Pollutants**

| | rhodamine B | | phenol | |
|---|---|---|---|---|
| catalyst | $K$ ($h^{-1}$) | $R$ | $K$ ($h^{-1}$) | $R$ |
| $SnS_2$ | 0.5068 | 0.9470 | 0.1845 | 0.9916 |
| $SnS_2$-RGO | 2.2127 | 0.9949 | 0.4643 | 0.9895 |

$SnS_2$ (0.5 $h^{-1}$). This value for the composite is also ~2.5 times larger than pristine $SnS_2$ for the degradation of phenol.

Generally, the photocatalytic activity of a semiconductor is mainly ascribed to the photoabsorption ability in the available light energy region, the ability for the photocatalysts to adsorb target pollutants, and the separation and transporting rate of the photogenerated electrons and holes in the catalysts. To find out the reason for enhanced visible light photocatalytic activity of $SnS_2$-RGO composite compared to pristine $SnS_2$, the UV−vis diffuse reflectance spectrometer (DRS) was used to determine the band gap energy of the synthesized samples (Figure 8a). Compared to pristine $SnS_2$, $SnS_2$-RGO composite showed an increased absorption in both UV and visible range and an obvious red-shift in the band gap transition. The band gap energy of $SnS_2$-RGO composite and pristine $SnS_2$ can be calculated by the following formula: $\alpha h\nu = A(h\nu - E_g)^{n/2}$, where $\alpha$, $h$, $\nu$, $E_g$, and $A$ are the absorption coefficient, Planck constant, the light frequency, the band gap, and a constant, respectively. Among them, $n$ depends on the characteristics of the transition in a semiconductor (direct transition $n = 1$ and indirect transition $n = 4$). For pristine $SnS_2$ and $SnS_2$-RGO

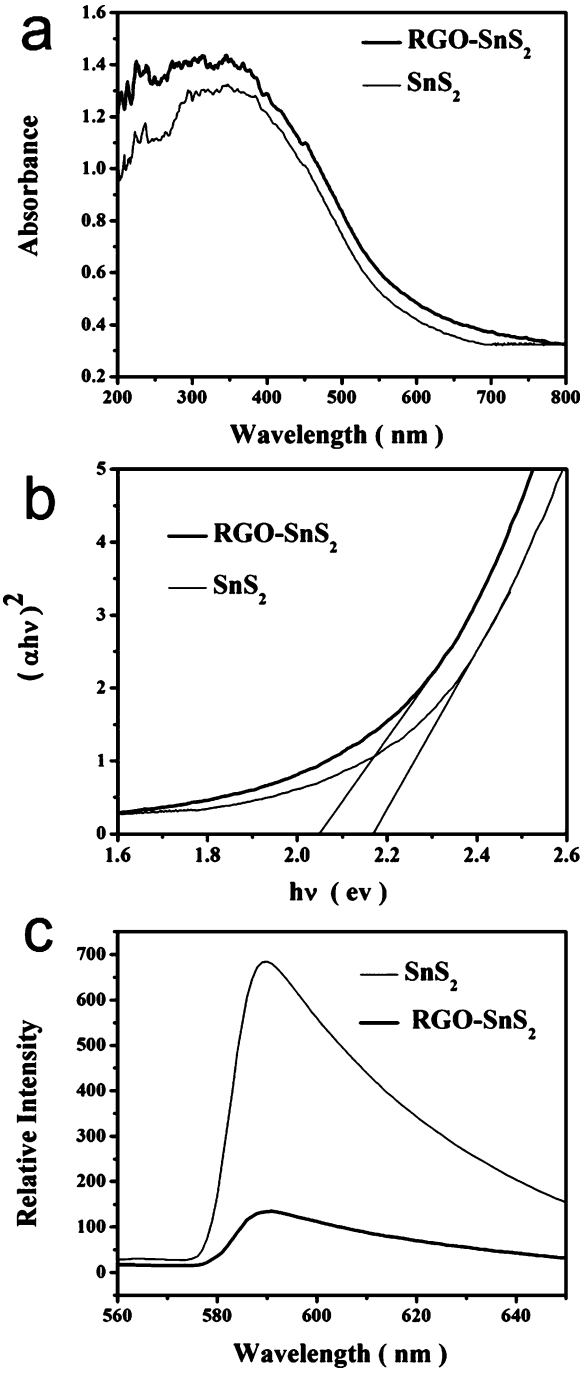


**Figure 8.** Pristine $SnS_2$ and $SnS_2$-RGO composite: (a) diffuse reflectance spectra, (b) plots of $(\alpha h\nu)^2$ vs $(h\nu)$, and (c) photoluminescence (PL) emission spectra.

composite, the value of $n$ is 1 for the direct transition. Consequently, the band gap energy of them can be estimated from a plot $(\alpha h\nu)^2$ versus photon energy $(h\nu)$. The intercept of the tangent to the $X$ axis could provide a good approximation of the band gap energy (Figure 8b). The band gap of pristine $SnS_2$ was evaluated to be 2.17 eV, whereas the band-gap of $SnS_2$-RGO composite was reduced to 2.05 eV. This phenomenon could be attributed to the chemical bonding between $SnS_2$ and the specific sites of RGO. The narrower band gap of $SnS_2$-RGO composite indicates the enhanced ability to absorb visible light, which is beneficial to the photocatalytic performance.

The recombination rate of the photo-induced electrons and holes are considered to be an important factor to influence the photocatalytic activity of materials. To investigate the efficiency of charge carrier trapping, immigration, and transfer in the as-prepared pristine $SnS_2$ and $SnS_2$-RGO composite, the photoluminescence (PL) emission spectra of these samples were measured (Figure 8c). An emitting peak at ~590 nm was observed for pristine $SnS_2$ when excited by 390 nm laser. Although peaks shapes and positions of $SnS_2$-RGO composite are similar to pristine $SnS_2$, the emission intensity of the composite is decreased significantly, which indicates that the recombination of photogenerated electrons and holes in $SnS_2$-RGO composite is inhibited greatly. RGO has superior electrical conductivity, which should make it an excellent electron-transport material in the photocatalytic process. The photogenerated electrons of excited $SnS_2$ are transferred instantly from the conduction band of $SnS_2$ to RGO, resulting in a minimized charge recombination and offering an enhanced photocatalytic activity. Moreover, it is generally accepted that the catalytic process is related to the adsorption of reactant molecules on the surface of catalyst. The surface area of $SnS_2$-RGO composite was calculated using $N_2$ adsorption to be 92.1 $m^2\ g^{-1}$, which is about 4 times of that of pristine $SnS_2$ (22.3 $m^2\ g^{-1}$). The higher specific surface area can result in a more unsaturated surface coordination sites exposed to the solution and enlarge the absorption of reactant molecules, thus enhancing the photocatalytic efficiency.

## 4. CONCLUSION

In summary, a new structure, namely graphene supported interconnected $SnS_2$ nanosheets, was designed and prepared by a one-step microwave-assisted technique. As an anode material for lithium ion battery, the composite also showed large reversible capacity and good cycling performance at 0.1 $C$ and unprecedented high-rate capability in terms of large capacity and high-rate cycling performance at 1 $C$ and 5 $C$. The $SnS_2$-RGO sheet-on-sheet composite was also demonstrated for the first time as a photocatalyst. The composite displayed excellent higher photocatalytic activity under visible light irradiation than pristine $SnS_2$ nanoflowers for the degradation of rhodamine B (RhB) and phenol. The mechanism for improved Li-ion storage properties and photocatalytic performances was also suggested and has been basically ascribed to the complementary effect of RGO and $SnS_2$ in the unique sheet-on-sheet nanostructure.

## ■ ASSOCIATED CONTENT

### Ⓢ Supporting Information

The XRD patterns of graphene oxide (GO) and reduced graphene oxide (RGO). The first cycle discharge and charge curves of $SnS_2$ and $SnS_2$-RGO composite at a current rate of 1 C. The cyclic voltammograms results and the high-rate cycling performances of $SnS_2$-RGO composite. The pollutant absorption rates of pristine $SnS_2$ and $SnS_2$-RGO composite. This material is available free of charge via the Internet at http://pubs.acs.org.

## ■ AUTHOR INFORMATION

### Corresponding Authors

*Phone: +86-21-66137723. Fax: +86-21-66137725. E-mail: yongwang@shu.edu.cn.
*E-mail: liuhong@shu.edu.cn.

### Notes

The authors declare no competing financial interest.

## ■ ACKNOWLEDGMENTS

The authors gratefully acknowledge the financial support from the follow-up Program for Professor of Special Appointment (Eastern Scholar), National Natural Science Foundation of China (51271105), and Shanghai Municipal Government (11YZ15, 11JC1403900, 11SG38, 12ZR1410300, S30109).

## ■ REFERENCES

(1) Mukaibo, H.; Yoshizawa, A.; Momma, T.; Osaka, T. *J. Power Sources* **2003**, *119*, 60−63.
(2) Momma, T.; Shiraishi, N.; Yoshizawa, A.; Osaka, T.; Gedanken, A.; Zhu, J.; Sominski, L. *J. Power Sources* **2001**, *97*, 198−200.
(3) Hong, S. Y.; Popovitz-Biro, R.; Prior, Y.; Tenne, R. *J. Am. Chem. Soc.* **2003**, *125*, 10470−10474.
(4) Zhai, C.; Du, N.; Zhang, H.; Yang, D. *Chem. Commun.* **2011**, *47*, 1270−1272.
(5) Ma, J.; Lei, D.; Mei, L.; Duan, X.; Li, Q.; Wang, T.; Zheng, W. *CrystEngComm* **2012**, *14*, 832−836.
(6) Du, Y.; Yin, Z.; Rui, X.; Zeng, Z.; Wu, X. J.; Liu, J.; Zhu, Y.; Zhu, J.; Huang, X.; Yan, Q.; Zhang, H. *Nanoscale* **2013**, *5*, 1456−1459.
(7) Dai, G.; Zou, B.; Wang, Z. *J. Am. Chem. Soc.* **2010**, *132*, 12174−12175.
(8) Radovsky, G.; Popovitz-Biro, R.; Staiger, M.; Gartsman, K.; Thomsen, C.; Lorenz, T.; Seifert, G.; Tenne, R. *Angew. Chem., Int. Ed.* **2011**, *123*, 12524−12528.
(9) Radovsky, G.; Popovitz-Biro, R.; Tenne, R. *Chem. Mater.* **2012**, *24*, 3004−3015.
(10) Zai, J.; Qian, X.; Wang, K.; Yu, C.; Tao, L.; Xiao, Y.; Chen, J. *CrystEngComm* **2012**, *14*, 1364−1375.
(11) Ma, J.; Lei, D.; Duan, X.; Li, Q.; Wang, T.; Cao, A.; Mao, Y.; Zheng, W. *RSC Adv.* **2012**, *2*, 3615−3617.
(12) Zai, J.; Wang, K.; Su, Y.; Qian, X.; Chen, J. *J. Power Sources* **2011**, *196*, 3650−3654.
(13) Xia, J.; Li, G.; Mao, Y.; Li, Y.; Shen, P.; Chen, L. *CrystEngComm* **2012**, *14*, 4279−4283.
(14) Kim, T. J.; Kim, C.; Son, D.; Choi, M.; Park, B. *J. Power Sources* **2007**, *167*, 529−535.
(15) Zhong, H.; Yang, G.; Song, H.; Liao, Q.; Cui, H.; Shen, P.; Wang, C. X. *J. Phys. Chem. C* **2012**, *116*, 9319−9326.
(16) Zhang, Y. C.; Du, Z. N.; Li, K. W.; Zhang, M. *Sep. Purif. Technol.* **2011**, *81*, 101−107.
(17) Takeda, N.; Parkinson, B. A. *J. Am. Chem. Soc.* **2003**, *125*, 5559−5571.
(18) Li, J.; Wang, T.; Du, X. *Sep. Purif. Technol.* **2012**, *101*, 11−17.
(19) Wahnon, P.; Conesa, J. C.; Palacios, P.; Lucena, R.; Aguilera, I.; Seminovski, Y.; Fresno, F. *Phys. Chem. Chem. Phys.* **2011**, *13*, 20401−20407.
(20) Zhang, Y. C.; Du, Z. N.; Li, K. W.; Zhang, M.; Dionysiou, D. D. *ACS Appl. Mater. Interfaces* **2011**, *3*, 1528−1537.
(21) Lucena, R.; Fresno, F.; Conesa, J. C. *Appl. Catal., A* **2012**, *415*, 111−117.
(22) Yang, C.; Wang, W.; Shan, Z.; Huang, F. *J. Solid State Chem.* **2009**, *182*, 807−812.
(23) Li, X.; Zhu, J.; Li, H. *Appl. Catal., B* **2012**, *123*, 174−181.
(24) Du, W.; Deng, D.; Han, Z.; Xiao, W.; Bian, C.; Qian, X. *CrystEngComm* **2011**, *13*, 2071−2076.
(25) Zhang, Y. C.; Du, Z. N.; Li, S. Y.; Zhang, M. *Appl. Catal., B* **2010**, *95*, 153−159.
(26) Zhang, Y. C.; Li, J.; Xu, H. Y. *Appl. Catal., B* **2012**, *123*, 18−26.
(27) Zhang, Y. C.; Li, J.; Zhang, M.; Dionysiou, D. D. *Environ. Sci. Technol.* **2011**, *45*, 9324−9331.
(28) Lei, Y.; Song, S.; Fan, W.; Xing, Y.; Zhang, H. *J. Phys. Chem. C* **2009**, *113*, 1280−1285.
(29) Chao, J.; Xie, Z.; Duan, X.; Dong, Y.; Wang, Z.; Xu, J.; Liang, B.; Shan, B.; Ye, J.; Chen, D.; Shen, G. *CrystEngComm* **2012**, *14*, 3163−3168.
(30) Zhou, X.; Zhou, T.; Hu, J.; Li, J. *CrystEngComm* **2012**, *14*, 5627−5633.
(31) Zhang, Y. C.; Yao, L.; Zhang, G.; Dionysiou, D. D.; Li, J.; Du, X. *Appl. Catal., B* **2014**, *144*, 730−738.
(32) Chen, S. Q.; Wang, Y. *J. Mater. Chem.* **2010**, *20*, 9735−9739.
(33) Lu, L. Q.; Wang, Y. *J. Mater. Chem.* **2011**, *21*, 17916−17921.
(34) Zou, Y.; Wang, Y. *Nanoscale* **2011**, *3*, 2615−2620.
(35) Chen, P.; Guo, L.; Wang, Y. *J. Power Sources* **2013**, *222*, 526−532.
(36) Zou, Y.; Kan, J.; Wang, Y. *J. Phys. Chem. C* **2011**, *115*, 20747−20753.
(37) Lu, L. Q.; Wang, Y. *Electrochem. Commun.* **2012**, *14*, 82−85.
(38) Wang, Z. L.; Xu, D.; Wang, H. G.; Wu, Z.; Zhang, X. B. *ACS Nano* **2013**, *7*, 2422−2430.
(39) Huang, X. L.; Wang, R. Z.; Xu, D.; Wang, Z. L.; Wang, H. G.; Xu, J. J.; Wu, Z.; Liu, Q. C.; Zhang, Y.; Zhang, X. B. *Adv. Funct. Mater.* **2013**, *23*, 4345−4353.
(40) Zhang, F. F.; Zhang, X. B.; Dong, Y. H.; Wang, L. M. *J. Mater. Chem.* **2012**, *22*, 11452−11454.
(41) Wang, H. G.; Wu, Z.; Meng, F. L.; Ma, D. L.; Huang, X. L.; Wang, L. M.; Zhang, X. B. *ChemSusChem* **2013**, *6*, 56−60.
(42) Wang, Z. L.; Xu, D.; Huang, Y.; Wu, Z.; Wang, L. M.; Zhang, X. B. *Chem. Commun.* **2012**, *48*, 976−978.
(43) Zou, Y.; Wang, Y. *ACS Nano* **2011**, *5*, 8108−8114.
(44) Sathish, M.; Mitani, S.; Tomai, T.; Honma, I. *J. Phys. Chem. C* **2012**, *116*, 12475−12481.
(45) Ji, L.; Xin, H. L.; Kuykendall, T. R.; Wu, S. L.; Zheng, H.; Rao, M.; Cairns, E. J.; Battaglia, V.; Zhang, Y. *Phys. Chem. Chem. Phys.* **2012**, *14*, 6981−6986.
(46) Yin, J.; Cao, H.; Zhou, Z.; Zhang, J.; Qu, M. *J. Mater. Chem.* **2012**, *22*, 23963−23970.
(47) Zhang, M.; Lei, D.; Yu, X.; Chen, L.; Li, Q.; Wang, Y.; Wang, T.; Cao, G. *J. Mater. Chem.* **2012**, *22*, 23091−23097.
(48) Shen, C.; Ma, L.; Zheng, M.; Zhao, B.; Qiu, D.; Pan, L.; Cao, J.; Shi, Y. *J. Solid State Electrochem.* **2012**, *16*, 1999−2004.
(49) Liu, S.; Lu, X.; Xie, J.; Cao, G.; Zhu, T.; Zhao, X. *ACS Appl. Mater. Interfaces* **2013**, *5*, 1588−1595.
(50) Chang, K.; Wang, Z.; Huang, G.; Li, H.; Chen, W.; Lee, J. Y. *J. Power Sources* **2012**, *201*, 259−266.
(51) Zhuo, L.; Wu, Y.; Wang, L.; Yu, Y.; Zhang, X.; Zhao, F. *RSC Adv.* **2012**, *2*, 5084−5087.
(52) Jiang, Z.; Wang, C.; Du, G.; Zhong, Y. J.; Jiang, J. Z. *J. Mater. Chem.* **2012**, *22*, 9494−9496.
(53) Jiang, X.; Yang, X.; Zhu, Y.; Shen, J.; Fan, K.; Li, C. *J. Power Sources* **2013**, *237*, 178−186.
(54) Luo, B.; Fang, Y.; Wang, B.; Zhou, J.; Song, H.; Zhi, L. *Energy Environ. Sci.* **2012**, *5*, 5226−5230.
(55) Novoselov, K. S.; Geim, A. K.; Morozov, S. V.; Jiang, D.; Zhang, Y.; Dubonos, S. V.; Grigorieva, I. V.; Firsov, A. A. *Science* **2004**, *306*, 666−669.
(56) Geim, A. K.; Novoselov, K. S. *Nat. Mater.* **2007**, *6*, 183−191.
(57) Wang, N.; Zhu, L.; Deng, K.; She, Y.; Yu, Y.; Tang, H. *Appl. Catal., B* **2010**, *95*, 400−407.
(58) Murugan, A. V.; Muraliganth, T.; Manthiram, A. *Chem. Mater.* **2009**, *21*, 5004−5006.
(59) Yoo, E.; Kim, J.; Hosono, E.; Zhou, H. S.; Kudo, T.; Honma, I. *Nano Lett.* **2008**, *8*, 2277−2282.
(60) Guo, P.; Song, H.; Chen, X. *Electrochem. Commun.* **2009**, *11*, 1320−1324.
(61) Gao, Z.; Liu, N.; Wu, D.; Tao, W.; Xu, F.; Jiang, K. *Appl. Surf. Sci.* **2012**, *258*, 2473−2478.
(62) Tao, W.; Chang, J.; Wu, D.; Gao, Z.; Duan, X.; Xu, F.; Jiang, K. *Mater. Res. Bull.* **2013**, *48*, 538−543.
(63) Fu, Y.; Chen, H.; Sun, X.; Wang, X. *Appl. Catal., B* **2012**, *111-112*, 280−287.

(64) Guo, S.; Zhang, G.; Guo, Y.; Yu, J. C. *Carbon* **2013**, *60*, 437−444.
(65) Min, Y.; Zhang, F. J.; Zhao, W.; Zheng, F.; Chen, Y.; Zhang, Y. *Chem. Eng. J.* **2012**, *209*, 215−222.
(66) Zhu, K.; Guo, L.; Lin, J.; Hao, W.; Shang, J.; Jia, Y.; Chen, L.; Jin, S.; Wang, W.; Chen, X. *Appl. Phys. Lett.* **2012**, *100*, 023113.
(67) Ma, H.; Shen, J.; Shi, M.; Lu, X.; Li, Z.; Long, Y.; Li, N.; Ye, M. *Appl. Catal., B* **2012**, *121- 122*, 198−205.
(68) Pradhan, G. K.; Padhi, D. K.; Parida, K. M. *ACS Appl. Mater. Interfaces* **2013**, *5*, 9101−9110.
(69) Chen, G.; Sun, M.; Wei, Q.; Zhang, Y.; Zhu, B.; Du, B. *J. Hazard. Mater.* **2013**, *244- 245*, 86−93.